Heliyon 10 (2024) e25426

Contents lists available at ScienceDirect

Heliyon

journal homepage: www.cell.com/heliyon

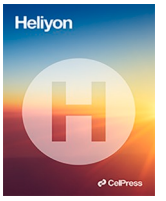

Research article

Si@Fe_3O_4/AC composite with interconnected carbon nano-ribbons network for high-performance lithium-ion battery anodes

Xiang Liu [a,b,*], Zhi Yu [a], Shan Fang [a], Yong Li [a], Guoxing Qu [a], Nai-Gen Zhou [a], Dong-Liang Peng [c,**]

[a] School of Physics and Materials Science, Nanchang University, Nanchang, 360031, China
[b] Ganfeng Lithium Group Co., Ltd. Xinyu 338015, China
[c] Department of Materials Science and Engineering, College of Materials, Xiamen University, Xiamen, 361005, China

ARTICLE INFO

Keywords:
Si nanoparticles
Anode
Carbon nano-ribbons
Electrochemical properties
Lithium-ion batteries

ABSTRACT

Si-based anode materials have a relatively high theoretical specific capacity and low operating voltage, greatly enhancing the energy density of rechargeable lithium-ion batteries (LIBs). However, their practical application is seriously hindered by the instability of active particles and anode electrodes caused by the huge swelling during cycling. How to maintain the stability of the charge transfer network and interface structure of Si particles is full of challenges. To address this issue, we have developed a novel Si@Fe_3O_4/AC/CNR anode by in-situ growing one-dimensional high elastic carbon nano-ribbons to wrap Si nanoparticles. This special structure can construct fast channels of electron transport and lithium ion diffusion, and stabilize the surface structure of Si nanoparticles during cycling. With these promising architectural features, the Si@Fe_3O_4/AC/CNR composite possesses a high specific capacity of 1279.4 mAh/g at 0.5 A/g, and a superior cycling life with 80 % capacity retention after 700 cycles. Even at a high current density of 20.0 A/g, the composite still delivers a capacity of 621.2 mAh/g. The facile synthetic approach and high performance of Si@Fe_3O_4/AC/CNR anodes provide practical insight into advanced anode materials with large volume expansion for high-energy-density LIBs.

1. Introduction

Over the last decade, lithium-ion batteries (LIBs) have been the major power source for commercial electric vehicles (EVs) and the main energy-storing device on the grid due to their small volume occupancy, long lifespan, and relatively safe [1,2]. Compared with K-ion batteries and zinc-ion batteries, LIBs are the most successful commercial batteries in current stage [3–5]. Developing high energy density LIBs to solve the problem of a limited driving range of EVs is the urgent demand for consumers and the main challenge for researchers [6–9]. However, the commercial graphite anodes have already approached the theoretical capacity (372 mAh/g), which is hard to fulfill the current high energy density demands [10,11]. Silicon-based anodes with the desirable features of high theoretical specific capacity and low operative potential are seen as an alternative anode material for the next generation LIBs [12–15]. However,

* Corresponding author. School of Physics and Materials Science, Nanchang University, Nanchang, 360031, China.
** Corresponding author.
E-mail addresses: liuxiang@ncu.edu.cn (X. Liu), dlpeng@xmu.edu.cn (D.-L. Peng).

https://doi.org/10.1016/j.heliyon.2024.e25426
Received 23 October 2023; Received in revised form 12 January 2024; Accepted 26 January 2024
Available online 28 January 2024

the severe shortcomings of its poor intrinsic electronic conductivity (10^{-3} S•cm^{-1}) and low Li^+ transfer number (10^{-14}~10^{-13} cm^2 s^{-1}) make Si anode suffer from limited C-rate capability [16–19]. More importantly, another fatal flaw of Si anode is mainly from the huge volume change (about 300 %) that occurs in the Li^+ insertion/extraction processes, which caused the cracking of active particles, electrode pulverization, and unstable solid electrolyte interphase (SEI) layers [20–23]. So, the aforementioned shortcomings of Si-based anodes should be overcome to implement their practical applications.

To improve the electrochemical properties of Si-based anodes, tremendous strategies were conducted to stabilize the microstructure, including nanocrystallization, hollow or porous construction, and application of carbonaceous material [24–31]. One of the most effective methods is to combine the Si nanoparticles and carbonaceous materials because it has several advantages to improve the performance of LIBs. Firstly, the carbon matrix can act as a buffering matrix to accommodate the swelling of Silicon nanoparticles during cycling. Secondly, it can accelerate the electronic transmission through the whole electrode. Thirdly, it can construct the efficient Li^+ and e^- transport path among the electrodes. There are three forms of carbon materials to wrap the Si nanoparticles including zero-dimensional carbon (0D) coating layer, one-dimensional (1D) carbon materials, and two-dimensional (2D) graphene host [32–36]. 1D carbonaceous materials (such as carbon nanotubes, and carbon fiber) have good electron transport characteristics and mechanical properties. Even though cracks appear on the surface of active particles or contact between particles is lost, electrons can still be transmitted in the active particles through the "bridge" of 1D carbon materials to improve the charge transfer limits by structural damage of active particles and electrodes. Ren et al. utilized the functionalized CNT to encapsulate the layered porous silicon for an ultra-stable anode with a high specific capacity and long cycling life [37]. Fang et al. proposed a flexible nanotemplate composed of short carbon nanotubes and small graphene flakes to closely wrap micron-sized mesoporous silicon [38]. Hong et al. prepared SiPAC/CNT-film anode with the CNT network, the excellent bendability of anodes makes the full cell maintain more than 96 % capacity after 10,000 times of 90° bending [39]. Lee et al. proposed a promising composite Si–Cu_3Si-CNT/G-C, which possesses high-capacity and long cycling life due to the multiple carbon network matrices [40]. However, 1D conductive nanomaterials have a large length/diameter ratio and high surface energy which lead to the agglomeration of materials. It is a challenge to wrap silicon particles with one-dimensional carbon nanomaterials only through a direct physical mixture.

The *in-situ* growth of 1D CNTs nanomaterials to encapsulate the Si nanoparticles is a good way to improve the dispersity and keep with a good interfacial configuration [41,42]. Hu et al. in situ synthesized Si/CNTs/C integrated anodes with the specific capacity of 1226 mAh/g after the 50th cycling at 50 mA/g due to CNTs acting as a "reinforcing bar" fixing Si active particles tightly [43]. Tian et al. designed hollow-structured SiOx@CNTs/C architectures with in situ growth of 1D CNTs and graphitic carbon coatings, and the SiOx@CNTs/C anodes exhibit superior electrochemical performances [44]. Nevertheless, the *in-situ* growth of 1D CNTs tends to utilize transition metals (Fe, Co, and Ni) as catalysts which could accelerate the decomposition of electrolytes and the self-discharge of cells. So, the acid etching process is inevitable.

Inspired by *in-situ* growing 1D CNTs on the surface of a metal catalyst, we designed a one-pot procedure to fabricate Si@Fe_3O_4/AC composites with self-assembly inter-connected carbon nano-ribbons (CNRs) networks. The Fe_3O_4 nanoparticles not only acted as catalysts to convert the amorphous carbon into CNRs but also offered additional capacity for the prepared anodes. The formed CNRs interconnected with each other and construct a 3D conductive network which improves the C-rate properties. Due to the excellent mechanical properties of CNRs and the buffer layer of amorphous carbon matrix, the Si and Fe_3O_4 nanoparticles wrapped with conductive CNRs as anode materials in LIBs exhibit a high cycling stability (retaining a reversible capacity of 913.6 mAh/g after 1000 cycles, still higher than graphite) and outstanding C-rate properties (possessing a reversible capacity of 621.2 mAh/g even at high current density of 20.0 A/g).

2. Experimental section

2.1. Synthesis of Si@/Fe_3O_4/AC/CNR

1 g glucose (as carbon source) and 0.73 g $Fe(NO_3)_3$•$9H_2O$ were dissolved in 10 mL deionized water, and then mixed with 600 mg commercial Si nanoparticles (~100 nm, Aladdin, Inc.) and stirred at room temperature. Then 15 g sodium chloride (NaCl) as a hard template was added into the solution. The mixture was transferred to a vacuum drying oven at 80 °C for 24 h to evaporate the excess water. Subsequently, the obtained mixture was ground into very fine powders and poured into a porcelain boat. After that, the fine powders were heated at 750 °C for 2 h at the heating rate of 5 °C•min^{-1} and then cooled to room temperature under an inert gas atmosphere. Washing the black powders with deionized water and ethanol several times to remove the hard template, and finally dried in a vacuum oven at 60 °C for one day. For comparison, Si/amorphous carbon, denoted as Si/AC, was prepared without $Fe(NO_3)_3$•$9H_2O$ at the same conditions as for the fabrication of the Si@Fe_3O_4/AC/CNR.

2.2. Material characterization

The X-ray diffraction curves of the samples were obtained by X-ray powder diffraction (XRD) on a Bruker-Axe X-ray diffractometer (fitted with Cu Kα). The micro morphologies of the prepared samples were studied by a field-emission scanning electron microscope (SEM) equipped with an energy-dispersive X-ray spectrometer. Transmission electron microscopy (TEM, JEM-2100, 200 kV) was used to study the microstructure of the obtained materials. The valence states of the elements of the as-prepared samples were detected by X-ray photoelectron spectroscopy (XPS, PHI Quantun-2000 spectrometer). The carbon content of Si@Fe_3O_4/AC/CNR and Si/AC composite was obtained on an SDT-Q600 thermal analyzer at a temperature range of room temperature to 750 °C with a heating rate of 10 °C/min.

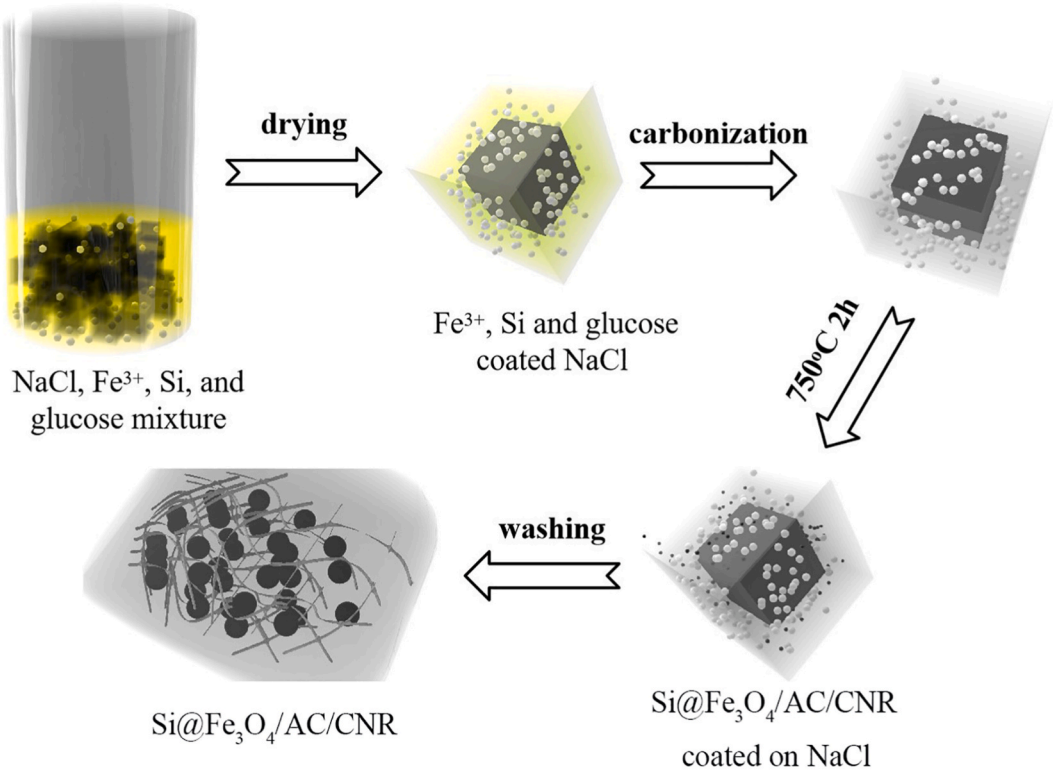

Fig. 1. Schematic diagram of the synthetic process of Si@Fe_3O_4/AC/CNR composite.

2.3. Electrochemical measurements

The as-prepared active materials, acetylene black and carboxymethyl cellulose (CMC) binder with a weight ratio of 7:2:1 in deionized water were intensely stirred overnight to form a homogeneous slurry. The working electrodes were formed by coating the slurry on a copper foil and drying it at 80 °C in a vacuum overnight. The loading mass of active material Si/AC was controlled to be 1.05 mg and the loading density is 0.93 mg cm^{-2}. The active material loading mass of Si@Fe_3O_4/AC/CNR was 1.19 mg and the loading density is 1.05 mg cm^{-2}. The counter electrode and reference electrode were lithium metal foil with a thickness of 1.2 mm. The coin cells (2025-type) were assembled in an Ar-filled glove box, using Celgard 2400 as the separator and 1 M $LiPF_6$ dissolved in a solvent of ethylene carbonate (EC) and diethyl carbonate (DEC) (1:1, vol%) as the electrolyte, respectively. Cyclic voltammetry (CV) evaluations and electrochemical impedance spectroscopy (EIS) were operated on the Chenhua CHI604E electrochemical workstation at room temperature. The galvanostatic discharge-charge test was conducted on a Neware battery test system.

3. Results and discussion

The synthetic process of Si@Fe_3O_4/AC/CNR composite is shown in Fig. 1. Firstly, Fe precursor, glucose, and Si nanoparticles were coated onto the surface of the hard template (NaCl microparticles) which is thermally stable. Secondly, while heating to 150 °C in a tube furnace at Ar atmosphere, the glucose granules started to melt and formed a thin liquid film which would adsorb onto the surface of NaCl. As the heating process proceeded, the Fe precursor reacted with glucose to form iron oxide nanoparticles. At this point, the amorphous carbon matrix was formed by the carbonization of the liquid organic carbon source film. When heating up to 750 °C, the formation of the carbon nano-ribbons network will be started at the interface between the amorphous carbon matrix and the iron oxide nanoparticles. It can be seen as a carbon graphitization process. The transition metal iron oxide nanoparticles act as a crucial catalyst in the formation of carbon nano-ribbons. A layer of graphene sheet is precipitated on the surface of the iron nanoparticle and starts to form a skeleton of graphite, the catalyst iron can convert neighboring free-state carbon atoms to graphite and then grow carbon nano-ribbons [45]. After washing the NaCl templates with deionized water, the Si@Fe_3O_4/AC/CNR composite with interconnected carbon nano-ribbons networks was obtained.

To verify the crystallographic phase composition and carbon state, the as-prepared samples were studied by XRD and Raman measurements. The XRD patterns of the as-prepared Si@AC and Si@Fe_3O_4/AC/CNR are shown in Fig. 2(a). It can be found that the Si@AC and Si@Fe_3O_4/AC/CNR samples have three main diffraction peaks at 28.4°, 47.3°, and 56.1°, corresponding with the cubic-phase silicon (JCPDS 27–1402) [46]. Without the Fe element, the glucose was carbonized to the amorphous carbon, so there is a broad amorphous peak at about 25.0° of Si@AC sample [41,47]. After adding Fe precursor, the characteristic peaks at 30.4° and 35.8° of the

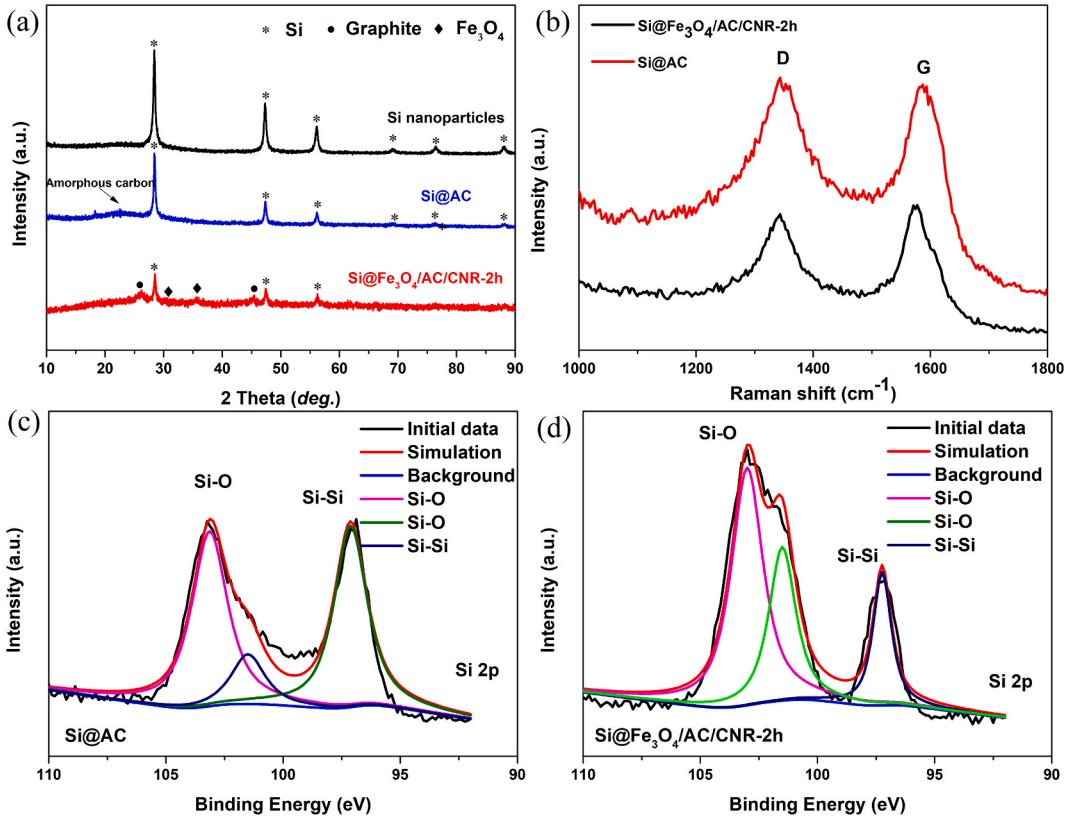

Fig. 2. (a) The XRD patterns, (b) Raman spectrum, (c–d) XPS spectrum of Si 2p peak (fitted with different component peaks) of the synthesized Si@AC and Si@Fe_3O_4/AC/CNR.

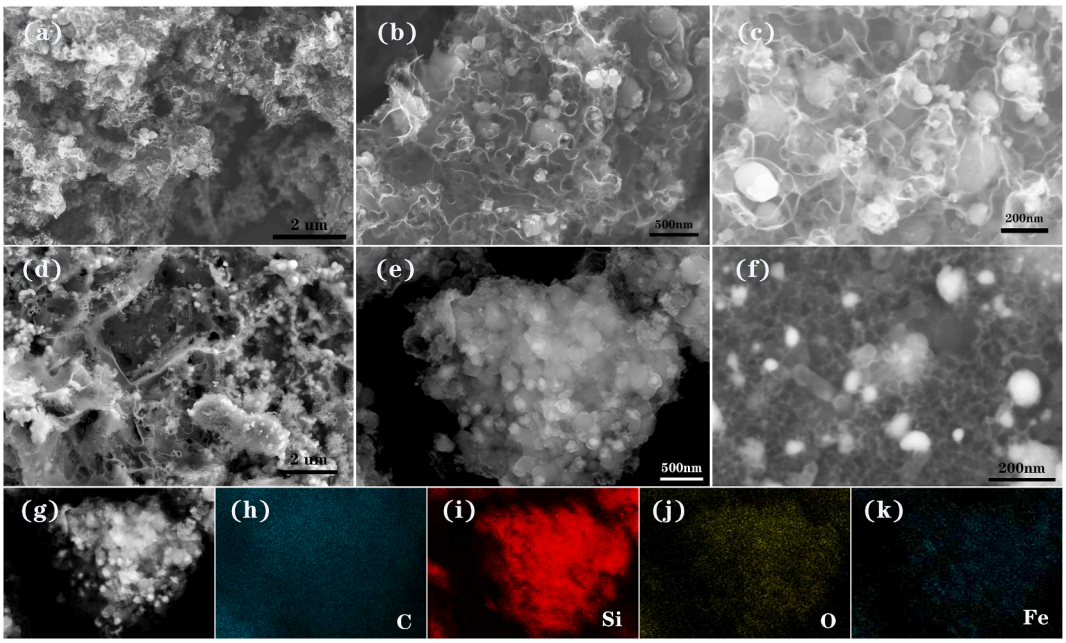

Fig. 3. FESEM images of the as-prepared Si@AC sample (a–c), Si@Fe_3O_4/AC/CNR composite (d–f), and the corresponding elemental mapping images of C (h), Si (i), O (j), and Fe (k).

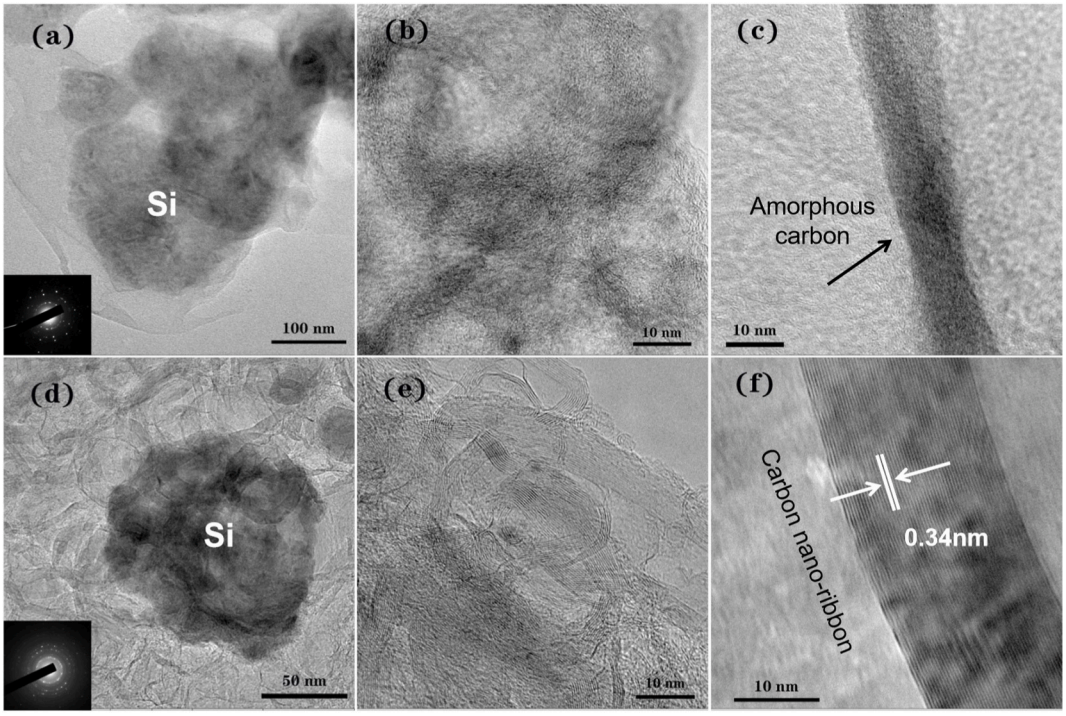

Fig. 4. The TEM images of Si@AC (a–c) and Si@Fe_3O_4/AC/CNR (d–f), the insets in (a) and (d) are SAED patterns of corresponding Si nanoparticles, (e) and (f) are the high-resolution TEM images of carbon in Si@AC and Si@Fe_3O_4/AC/CNR composite.

sample are determined for (220) and (311) lattice planes of cubic structure magnetite (JCPDS 01-075-0449) [48,49]. Remarkably, there is an obvious peak at 26.4° which belongs to the graphitic carbon [43,50]. Notably, the intensity of the silicon diffraction peak becomes weaker maybe due to the oxidation of Si nanoparticles during the heating process. Raman spectra further confirm the higher graphitization degree of Si@Fe_3O_4/AC/CNR composite than Si@AC sample. As shown in Fig. 2(b), the peaks located at 1345.6 cm^{-1} and 1585.5 cm^{-1} are assigned as the D band and G band of the carbon in Si@AC and Si@Fe_3O_4/AC/CNR composite, respectively. Based on the fitted D and G band, the I_D/I_G ratio of Si@Fe_3O_4/AC/CNR composite (0.90) is lower than Si@AC (1.06) which means that the highly ordered structure due to form the CNRs [51]. The electrical conductivity of carbon materials is related to the graphitization degree in a heating process. It means that the Si@Fe_3O_4/AC/CNR sample has better electron conductivity [45]. The binding energy peaks of Si 2p were found in the sample of Si@AC and Si@Fe_3O_4/AC/CNR by X-ray photoelectron spectroscopy (XPS) in Fig. 2(c and d). Apart from the Si 2p peak at 97.1 eV corresponds to the Si–Si bond, there are another two peaks located at 103.1eV and 101.5 eV which correspond to the Si–O bond, owing to the partial oxidation on the surface of the Si nanoparticles [12,52–54]. For the Si@Fe_3O_4/AC/CNR composite, the intensity of the Si–O peak is increasing means that the Si nanoparticles have a thicker oxidation coating than the Si@AC composite, and the result is by the XRD patterns.

The morphologies of the synthesized Si@AC and Si@Fe_3O_4/AC/CNR are investigated by FESEM in Fig. 3(a–c) and Fig. 3(d–f), respectively. Both samples possess a 3D hierarchical structure with the Si nanoparticles embedded in the carbon matrix. Compared with the Si@AC sample, the Si@Fe_3O_4/AC/CNR composite exhibits a rough and crinkle-like surface. To further confirm the distribution of individual elements of Si@Fe_3O_4/AC/CNR composite, the corresponding elemental mapping images are presented in Fig. 3 (g–k). In the selected sample area, the individual elemental maps of C, Si, O, and Fe present a uniform distribution. The EDS result shows that the contents of C, O, Si, and Fe are 14.55, 23.82, 49.65, and 11.98 wt%, respectively.

To capture more morphologies detail, transmission electron microscopy (TEM) is carried out to further study the microstructure of the as-prepared Si@AC and Si@Fe_3O_4/AC/CNR composite. As shown in Fig. 4(a–c), the Si nanoparticles size is about 100 nm and enveloped in the amorphous carbon matrix. For Si@Fe_3O_4/AC/CNR composite, the Si nanoparticle is wrapped by the interconnected carbon nano-ribbons. The carbon nano-ribbons are intertwined and connected in Fig. 4(d and e). The multi-layer structure of graphite was observed in the nano-ribbons as shown in Fig. 4(f), and the width of the carbon nano-ribbons varied from a few to a dozen nanometers. It appears that the carbon nano-ribbons are formed when the precursor adds iron nitrate. So iron nanoparticles play a crucial role in catalyzing the synthesis of carbon nano-ribbons from the bulk amorphous carbon. The formation mechanism of carbon nano-ribbons is analogous to a carbon graphitization process. When a graphene layer is precipitated onto the surface of the iron oxide nanoparticle, a skeleton of graphite forms, then the iron oxide nanoparticle can play a catalytic role in converting spatially connected amorphous carbon to graphite and a source to grow carbon nano-ribbons. The microstructure of the as-synthetized Si@Fe_3O_4/AC/CNR composite with interconnected carbon nano-ribbon networks constructs a three-dimensional electronic conductive network which could contribute to the rate performance of the Si-based anode. Si material is a semiconductor and has huge volume expansion during

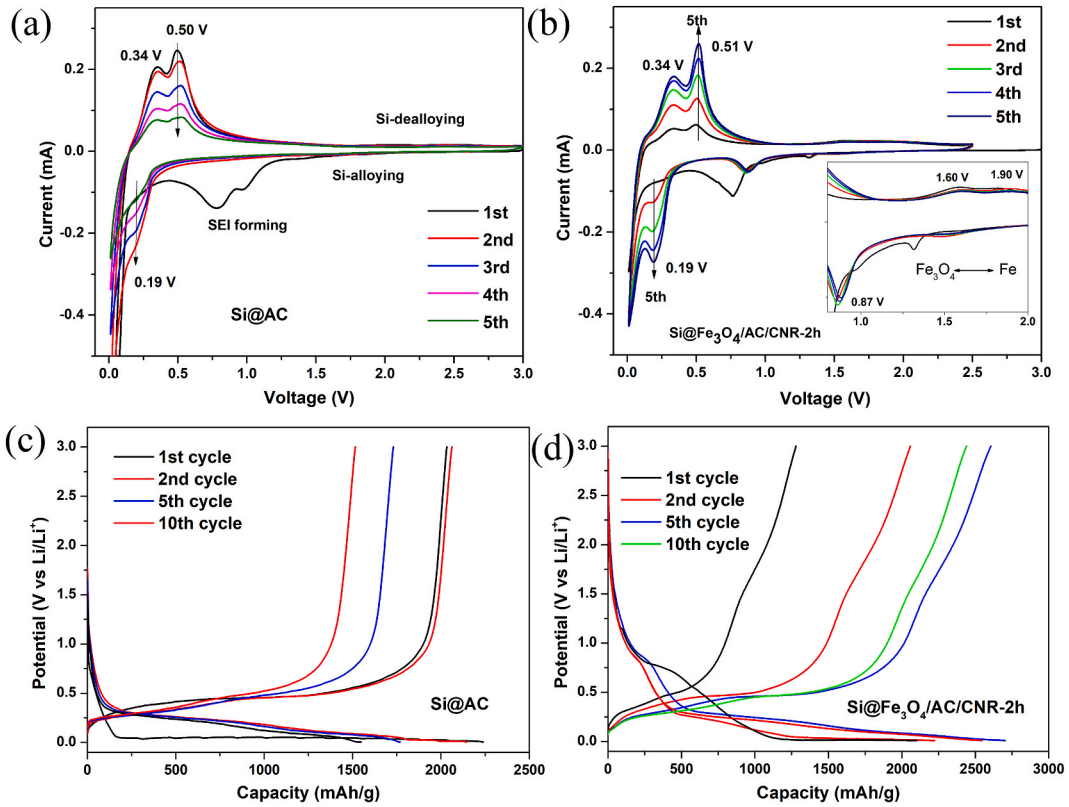

Fig. 5. (a) CV curves of Si@AC and (b) Si@Fe_3O_4/AC/CNR, (c) voltage profiles of the 1st, 2nd, 5th, and 10th cycle for Si@AC and Si@Fe_3O_4/AC/CNR (d) at a current density of 0.5 A/g.

the charging/discharging process which is not good for the stabilization of the electron conduction network of anode electrode. The one-dimensional carbon nano-ribbon can act as a "bridge" to maintain the electron transport in anode electrode even though the pulverization of Si particle happened.

The electrochemical performances of the Si@AC and Si@Fe_3O_4/AC/CNR electrodes after the pressing process were studied by assembling them into CR-2025 half-coin cells. From the cyclic voltammetry curves of the Si@AC and Si@Fe_3O_4/AC/CNR composite in Fig. 5(a and b), the appearance of a wide peak at 0.78 V can be ascribed to the formation of SEI films during the initial cathodic scanning process. This irreversible reaction which causes capacity loss disappears in the next cycles. The peak at 0.19 V is assigned to the formation of amorphous Li_xSi alloys when Li^+ is inserted into Si nanoparticles. Furthermore, two anodic peaks at about 0.34 V and 0.50 V are in accordance with the reaction of the delithiation of Li_xSi alloys to form amorphous Si particles. The intensity of the reversible peak is creasing at the first five cycles for Si@Fe_3O_4/AC/CNR composite means that the anode needs an activation process to release all capacity. Compared with the Si@AC sample, there is a reversible cathodic peak at 0.87 V for the Si@Fe_3O_4/AC/CNR composite which belongs to the lithiation reaction of Fe_3O_4[55]. Correspondingly, two anodic peaks at about 1.60 V and 1.90 V in Fig. 5(b) during the charging process attributed to the electrochemical reactions ($Fe_3O_4 \leftrightarrow Fe$) as lithium-ion extraction [55,56]. It follows from the above that the Fe_3O_4 nanoparticles not only could act as the catalyst for carbon nano-ribbons formation, but also make contributions to increase the reversible capacity of the anode.

Fig. 5(c and d) shows the discharge/charge voltage curves of Si@AC and Si@Fe_3O_4/AC/CNR anodes at a current density of 0.5 A/g between 0.005 and 3.0 V. The Si@AC sample delivers a high Li^+ storage capacity of 2238.1 mAh/g during the initial Li^+ insertion process, but a relatively low reversible specific capacity of 2032.4 mAh/g is acquired, which means a relatively low initial coulombic efficiency (ICE) (90.8 %). For Si@Fe_3O_4/AC/CNR composite, the initial Li^+ insertion capacity is 2100.2 mAh/g and the Li^+ extraction capacity is 1279.4 mAh/g, due to the high irreversible capacity of Fe_3O_4 and partly oxidation of nano-Si, which lead to lower initial coulombic efficiency of 60.9 %. In addition, the BET test (Fig. S6) shows that the specific surface area of Si@Fe_3O_4/AC/CNR (17.02 m^2/g) is much larger than the Si@AC composite (10.88 m^2/g) which may induce more side reactions with the electrolyte and lead to a lower ICE. Unlike the Si@AC sample, there is a discharge voltage plateau around 0.8 V which belongs to the lithiation reaction of Fe_3O_4, in accord with the cathodic peak at 0.87 V of CV curves in Fig. 5(b). Moreover, a long discharge voltage plateau contributes to the major capacity of Si@Fe_3O_4/AC/CNR composite is ascribed to electrochemical intercalation characteristics of lithium-ion in Si nanoparticles. In the charging cycles, a short voltage plateau is observed at about 1.6 V which belongs to Fe_3O_4, in agreement with the previously reported in the literature for Fe_3O_4-based electrodes [55]. The reversible capacity of the Si@AC anode rapidly decreases while the discharge capacity of the Si@Fe_3O_4/AC/CNR anode increases during the first five cycles, the results in accordance with the

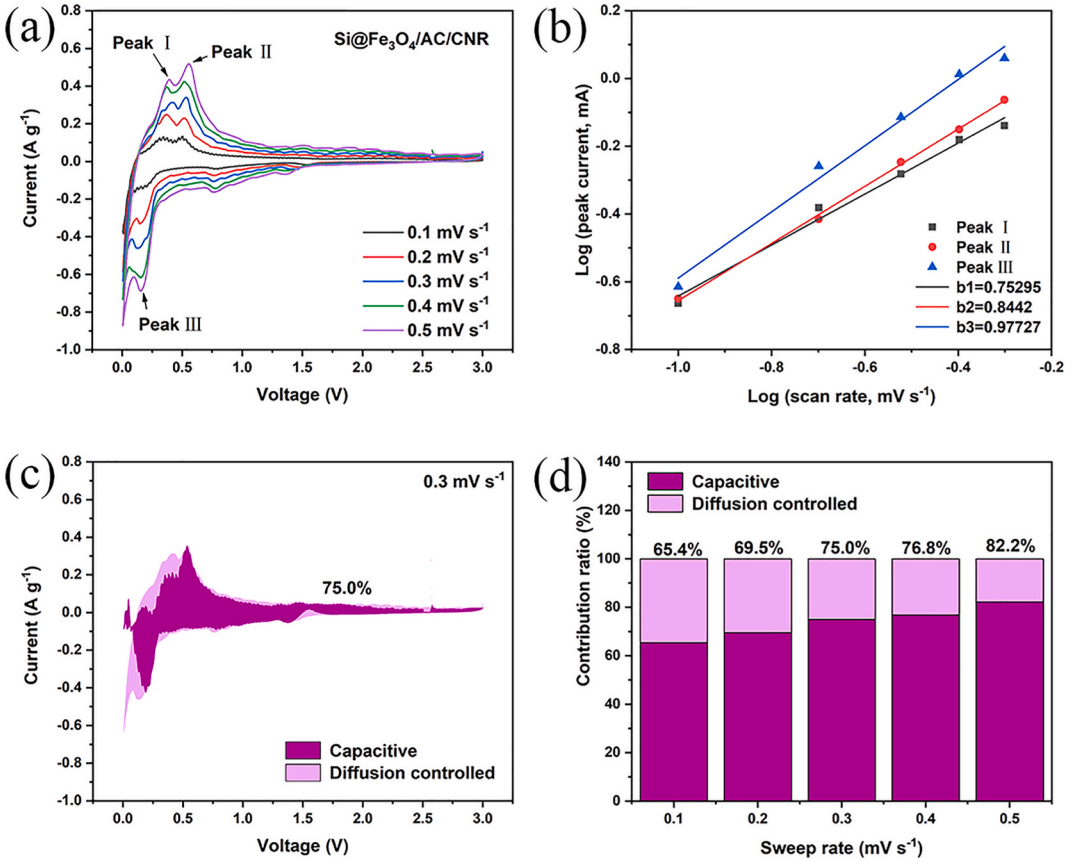

Fig. 6. The capacitive contribution of Si@Fe_3O_4/AC/CNR (a) CV curves at different scan rates, (b) log i versus log v plots at specific peak currents, (c) separation of the capacitive and diffusion-controlled current contribution at 0.3 mV s^{-1}. (d) The contribution ratio of the capacitive capacities and diffusion-limited capacities at different scan rates.

variation of the cathodic peak intensity in the CV curve.

Fig. 6(a–d) shows the capacity contribution of the Si@Fe_3O_4/AC/CNR anode electrodes. Fig. 6(b) shows the value of *b* between 0.5 and 1.0, illustrating that the capacity contribution originates from both surface and diffusion-controlled mechanisms. According to the calculation formula, the pseudocapacitive regime at 0.3 mV s is obtained in Fig. 6(c). With the contrast in Fig. 6(d), the contributions of pseudocapacitive reaction increase with the scan rate. This is more beneficial to the rate performance.

The cycling properties of pure Si nanoparticles, Si@AC, and Si@Fe_3O_4/AC/CNR electrodes at 0.5 A/g can be seen in Fig. 7(a). The pure Si nanoparticles exhibit rapid capacity fading in the first cycles due to the uncontrolled huge volume swelling. The cycling performance of Si@AC anodes could be partly improved due to higher electric conductivity and buffering of the amorphous carbon. Owing to the well-designed microstructure, the Si@Fe_3O_4/AC/CNR electrodes deliver a superior reversible specific capacity of 1963.7 mAh/g after 60 cycles with a capacity retention of 92.1 %. These results demonstrate that the one-dimensional graphene nano-ribbons give the electrons a highly conductive path and superior mechanical flexibility, which contributes to the improvement of the cycling performance of the Si anodes. Fig. 7(b) shows the rate performance of the Si@Fe_3O_4/AC/CNR electrodes, which deliver superior rate capability with average capacities of 2191.7 mAh/g, 2048.8 mAh/g, 1889.9 mAh/g, 1426.0 mAh/g, 908.7 mAh/g and 621.0 mAh/g at the current densities of 0.2, 0.5, 1.0, 5.0, 10.0, and 20.0 A/g. The discharge capacity can recover to 1711.1 mAh/g when restoring to 0.2 A/g, which means that the structure of the Si@Fe_3O_4/AC/CNR electrode is not seriously destroyed even under ultrahigh current density.

The fast reaction kinetics of Si@Fe_3O_4/AC/CNR electrode is further supported by electrochemical impedance spectroscopy (EIS) measurement. The Nyquist plots of Si@AC and Si@Fe_3O_4/AC/CNR anodes before cycling are presented in Fig. 7(c and d). The high-frequency region and low-frequency region belong to the charge-transfer resistance and Warburg impedance, respectively. The Warburg impedance is associated with the Li^+ diffusion in the anode and the charge-transfer resistance (R_{ct}) is related to the double-layer capacitance on the electrode/electrolyte interface. According to the equivalent circuit model, the Si@Fe_3O_4/AC/CNR electrode delivers an R_{ct} value of 28.7 Ω which approximates the value of the Si@AC anode. After 1st cycle, the R_{ct} value of Si@AC increases to 119.8 Ω, which indicates that the Si particles emerge cracks and pulverization, and then the thick SEI layers grown at the fresh surface of Si anode block the charge transfer to the active particles. However, the R_{ct} value of Si@Fe_3O_4/AC/CNR anode is much lower than Si@AC, exhibiting 22.2 Ω after 120 cycles. The unique architecture of Si@Fe_3O_4/AC/CNR anode could stabilize the interior structure

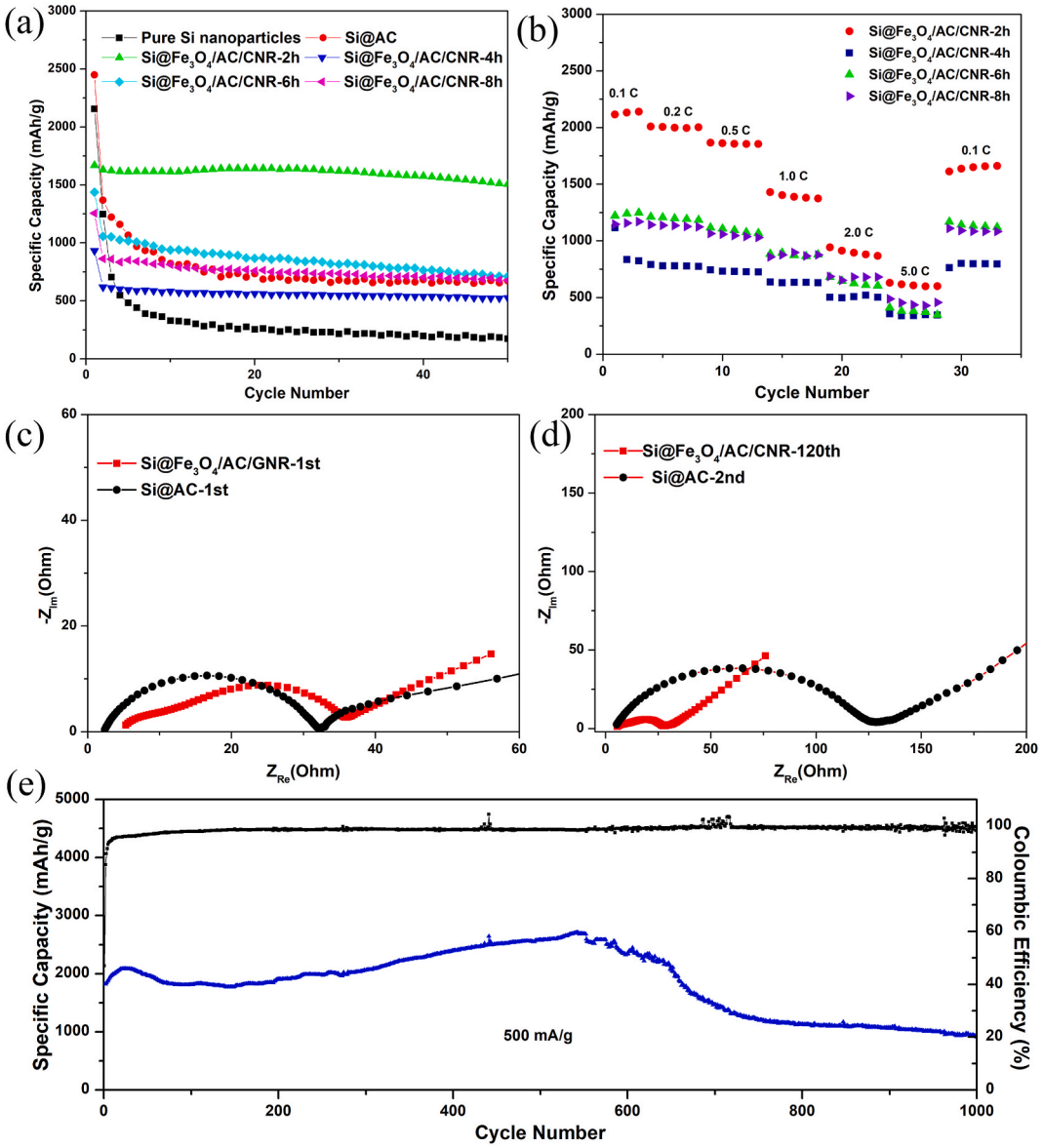

Fig. 7. (a) Cycling performance of Si nanoparticles, Si@AC and Si@Fe_3O_4/AC/CNR electrodes, (b) Rate performance of Si@Fe_3O_4/AC/CNR and Si@AC electrodes, (c–d) Nyquist plots of Si@AC and Si@Fe_3O_4/AC/CNR samples at different cycles, (e) Long-term cycling performance of the Si@Fe_3O_4/AC/CNR electrodes.

and interface of Si nanoparticles and inhibit the formation of SEI during cycling.

The long cycling at 0.5 A/g leads to a recovered capacity of 913.6 mAh/g after 1000 cycles in Fig. 7(e), still much higher than the commercial graphite anodes which could give a theoretical specific capacity of 372 mAh/g. The capacity of Si@Fe_3O_4/AC/CNR composite is increasing for a long cycle which may be due to the reversible formation of the polymeric gel-like film [57–59]. The conversion reaction product Fe nanoparticles after the discharge process could act as a catalyst to activate or promote some ingredient of SEI which contributes to the extra capacity [60]. Moreover, the large volume expansion of Si nanoparticles during the charging and discharging process and the insertion of lithium ions further exfoliate graphene layers, the freshly exposed active sites for extra lithium storage [61]. The Fe_3O_4 nanoparticles were etched by acid and the obtained Si/AC/CNR composite anode showed the same capacity fading behavior with Si@Fe_3O_4/AC/CNR composite (seen in Fig. S4). Due to the expansion of the Si nanoparticles, the uninfiltrated part of the anode tightly wrapped by the carbon nano-ribbons is reactivated and shows a continuously increasing capacity during the long cycling. Compared to the other Si-based anodes wrapped with 1D or 2D conductive carbon materials, the Si@Fe_3O_4/AC/CNR electrode have superior electrochemical performance (Table S1). Benefiting from the efficient electronic conductive network constructed by the 1D carbon nano-ribbons and amorphous carbon matrix, which also effectively buffer the volume swelling of the active materials during the (de)lithiation, the Si@Fe_3O_4/AC/CNR anode shows excellent cycle life.

4. Conclusions

In conclusion, the unique Si@Fe_3O_4/AC/CNR composite was successfully synthesized by a facile solution phase, followed by a carbonization process. The Fe element not only acts as the catalyst for forming carbon nano-ribbons but also contributes to lithium storage capability. Compared with the pure Si nanoparticles and Si@AC samples, the electrochemical properties of Si@Fe_3O_4/AC/CNR electrode have been greatly improved by enveloping Si nanoparticles in a CNR-reinforced fibrous network. Designing a 3D conductive network composed of the amorphous carbon matrix and 1D carbon nano-ribbons not only alleviates the volume swelling of Si particles but also enhances electronic conductivity. As the anodes of LIBs, Si@Fe_3O_4/AC/CNR electrode exhibits a superior reversible capacity of 913.6 mAh/g after 1000 cycles, and an excellent rate capability of 621 mAh/g at the current densities of 20.0 A/g. Therefore, the rational structural design of the CNR-reinforced conductive network can effectively improve the electrochemical properties of Si-based anodes.

CRediT authorship contribution statement

Xiang Liu: Writing – review & editing. **Zhi Yu:** Validation, Investigation, Formal analysis. **Shan Fang:** Writing – review & editing. **Yong Li:** Writing – review & editing, Formal analysis. **Guoxing Qu:** Formal analysis. **Nai-Gen Zhou:** Validation. **Dong-Liang Peng:** Writing – review & editing, Supervision, Conceptualization.

Declaration of competing interest

The authors declare that they have no known competing financial interests or personal relationships that could have appeared to influence the work reported in this paper.

Acknowledgments

This work was partially supported by the China Postdoctoral Science Foundation (Grant Nos. 2022M721421), Jiangxi Provincial Natural Science Foundation (Grant Nos. 20224BAB214011, 20212BAB214054, 20224BAB204011, 20212BAB214053 , 20223BBE51028), National Natural Science Foundation of China (52002176, 52161039).

Appendix A. Supplementary data

Supplementary data to this article can be found online at https://doi.org/10.1016/j.heliyon.2024.e25426.

References

[1] M. Li, J. Lu, Z. Chen, K. Amine, 30 Years of lithium-ion batteries, Adv. Mater. 30 (33) (2018) 1800561, https://doi.org/10.1002/adma.201800561.
[2] A. Tomaszewska, Z. Chu, X. Feng, S. O'Kane, X. Liu, J. Chen, C. Ji, E. Endler, R. Li, L. Liu, Y. Li, S. Zheng, S. Vetterlein, M. Gao, J. Du, M. Parkes, M. Ouyang, M. Marinescu, G. Offer, B. Wu, Lithium-ion battery fast charging: a review, eTransportation 1 (2019) 100011, https://doi.org/10.1016/j.etran.2019.100011.
[3] H. Liu, H. Du, W. Zhao, X. Qiang, B. Zheng, Y. Li, B. Cao, Fast Potassium migration in mesoporous carbon with ultrathin framework boosting superior rate performance for high-power potassium storage, Energy Storage Mater. 40 (2021) 490–498, https://doi.org/10.1016/j.ensm.2021.05.037.
[4] B. Cao, H. Liu, P. Zhang, N. Sun, B. Zheng, Y. Li, H. Du, B. Xu, Flexible mxene framework as A fast electron/potassium-ion dual-function conductor boosting stable potassium storage in graphite electrodes, Adv. Funct. Mater. 31 (32) (2021) 2102126, https://doi.org/10.1002/adfm.202102126.
[5] H. Liu, Z. Xin, B. Cao, Z. Xu, B. Xu, Q. Zhu, J. Yang, B. Zhang, H. Fan, Polyhydroxylated organic molecular additives for durable aqueous zinc battery, Adv. Funct. Mater. (2023) 2309840, https://doi.org/10.1002/adfm.202309840.
[6] X. Yang, Y. Huang, J. Li, W. Huang, W. Yang, C. Wu, S. Tang, F. Ren, Z. Gong, N. Zhou, Y. Yang, Understanding of working mechanism of lithium difluoro (oxalato) borate in Li||NCM85 battery with enhanced cyclic stability, Energy Nater 3 (2023) 300029, https://doi.org/10.20517/energymater.2023.10.
[7] Y.-Y. Sun, F. Li, P.-Y. Hou, Research progress on the interfaces of solid-state lithium metal batteries, J. Mater. Chem. A 9 (15) (2021) 9481–9505, https://doi.org/10.1039/D1TA00467K.
[8] D.T. Boyle, W. Huang, H. Wang, Y. Li, H. Chen, Z. Yu, W. Zhang, Z. Bao, Y. Cui, Corrosion of lithium metal anodes during calendar ageing and its microscopic origins, Nat. Energy (2021), https://doi.org/10.1038/s41560-021-00787-9.
[9] C. Wang, C. Yang, Z. Zheng, Toward practical high-energy and high-power lithium battery anodes: present and future, Adv. Sci. 9 (9) (2022) 2105213, https://doi.org/10.1002/advs.202105213.
[10] L. Zhao, B. Ding, X.-Y. Qin, Z. Wang, W. Lv, Y.-B. He, Q.-H. Yang, F. Kang, Revisiting the roles of natural graphite in ongoing lithium-ion batteries, Adv. Mater. 34 (18) (2022) 2106704, https://doi.org/10.1002/adma.202106704.
[11] S. Chae, S. Choi, N. Kim, J. Sung, J. Cho, Integration of graphite and silicon anodes for the commercialization of high-energy lithium-ion batteries, Angew. Chem. Int. Ed. 59 (1) (2020) 110–135, https://doi.org/10.1002/anie.201902085.
[12] A. Raza, J.Y. Jung, C.-H. Lee, B.G. Kim, J.-H. Choi, M.-S. Park, S.-M. Lee, Swelling-controlled double-layered SiO_x/Mg_2SiO_4/SiO_x composite with enhanced initial coulombic efficiency for lithium-ion battery, ACS Appl. Mater. Interfaces 13 (6) (2021) 7161–7170, https://doi.org/10.1021/acsami.0c19975.
[13] Z. Liu, Q. Yu, Y. Zhao, R. He, M. Xu, S. Feng, S. Li, L. Zhou, L. Mai, Silicon oxides: a promising family of anode materials for lithium-ion batteries, Chem. Soc. Rev. 48 (1) (2019) 285–309, https://doi.org/10.1039/C8CS00441B.
[14] D.H.S. Tan, Y.-T. Chen, H. Yang, W. Bao, B. Sreenarayanan, J.-M. Doux, W. Li, B. Lu, S.-Y. Ham, B. Sayahpour, J. Scharf, E.A. Wu, G. Deysher, H.E. Han, H. J. Hah, H. Jeong, J.B. Lee, Z. Chen, Y.S. Meng, Carbon-free high-loading silicon anodes enabled by sulfide solid electrolytes, Science 373 (6562) (2021) 1494–1499, https://doi.org/10.1126/science.abg7217.
[15] Z. Wang, Z. Xu, Y. Yuan, X. Teng, Z. Pu, Y. Wang, A. Fu, Y.-G. Guo, H. Li, Microspheres comprise Si nanoparticles modified with TiO_2 and wrapped by graphene as high-performance anode for lithium-ion batteries, Appl. Surf. Sci. 598 (2022) 153790, https://doi.org/10.1016/j.apsusc.2022.153790.

[16] M. Ko, S. Chae, S. Jeong, P. Oh, J. Cho, Elastic α -silicon nanoparticle backboned graphene hybrid as a self-compacting anode for high-rate lithium ion batteries, ACS Nano 8 (8) (2014) 8591–8599, https://doi.org/10.1021/nn503294z.

[17] Y. Hwa, W.-S. Kim, S.-H. Hong, H.-J. Sohn, High capacity and rate capability of core–shell structured nano-Si/C anode for Li-ion batteries, Electrochim. Acta 71 (2012) 201–205, https://doi.org/10.1016/j.electacta.2012.03.138.

[18] N. Ding, J. Xu, Y.X. Yao, G. Wegner, X. Fang, C.H. Chen, I. Lieberwirth, Determination of the diffusion coefficient of lithium ions in nano-Si, Solid State Ionics 180 (2–3) (2009) 222–225, https://doi.org/10.1016/j.ssi.2008.12.015.

[19] L. Tong, K. Long, L. Chen, Z. Wu, Y. Chen, High-capacity and long-lived silicon anodes enabled by three-dimensional porous conductive network design and surface reconstruction, ACS Appl. Energy Mater. (2022), https://doi.org/10.1021/acsaem.2c02500 acsaem.2c02500.

[20] S. Chae, M. Ko, K. Kim, K. Ahn, J. Cho, Confronting issues of the practical implementation of Si anode in high-energy lithium-ion batteries, Joule 1 (1) (2017) 47–60, https://doi.org/10.1016/j.joule.2017.07.006.

[21] Z. Xiao, C. Lei, C. Yu, X. Chen, Z. Zhu, H. Jiang, F. Wei, Si@Si_3N_4@C composite with egg-like structure as high-performance anode material for lithium ion batteries, Energy Storage Mater. 24 (2020) 565–573, https://doi.org/10.1016/j.ensm.2019.06.031.

[22] H. Wang, J. Fu, C. Wang, J. Wang, A. Yang, C. Li, Q. Sun, Y. Cui, H. Li, A binder-free high silicon content flexible anode for Li-ion batteries, Energy Environ. Sci. 13 (3) (2020) 848–858, https://doi.org/10.1039/C9EE02615K.

[23] Q. Xu, J.-Y. Li, J.-K. Sun, Y.-X. Yin, L.-J. Wan, Y.-G. Guo, Watermelon-inspired Si/C microspheres with hierarchical buffer structures for densely compacted lithium-ion battery anodes, Adv. Energy Mater. 7 (3) (2017) 1601481, https://doi.org/10.1002/aenm.201601481.

[24] H. Wu, P. Gao, J. Mu, Z. Miao, P. Zhou, T. Zhou, J. Zhou, Matryoshka-type carbon-stabilized hollow Si spheres as an advanced anode material for lithium-ion batteries, Chin. Chem. Lett. 33 (6) (2022) 3236–3240, https://doi.org/10.1016/j.cclet.2021.10.039.

[25] Q. Ma, Y. Dai, H. Wang, G. Ma, H. Guo, X. Zeng, N. Tu, X. Wu, M. Xiao, Directly conversion the biomass-waste to Si/C composite anode materials for advanced lithium ion batteries, Chin. Chem. Lett. 32 (1) (2021) 5–8, https://doi.org/10.1016/j.cclet.2020.11.007.

[26] L. Cao, T. Huang, Q. Zhang, M. Cui, J. Xu, R. Xiao, Porous Si/Cu anode with high initial coulombic efficiency and volumetric capacity by comprehensive utilization of laser additive manufacturing-chemical dealloying, ACS Appl. Mater. Interfaces 12 (51) (2020) 57071–57078, https://doi.org/10.1021/acsami.0c16887.

[27] Z. Zhang, Y. Wang, W. Ren, Q. Tan, Y. Chen, H. Li, Z. Zhong, F. Su, Scalable synthesis of interconnected porous silicon/carbon composites by the rochow reaction as high-performance anodes of lithium ion batteries, Angew. Chem. Int. Ed. 53 (20) (2014) 5165–5169, https://doi.org/10.1002/anie.201310412.

[28] J. Fu, H. Liu, L. Liao, P. Fan, Z. Wang, Y. Wu, Z. Zhang, Y. Hai, G. Lv, L. Mei, H. Hao, J. Xing, J. Dong, Ultrathin Si/CNTs paper-like composite for flexible Li-ion battery anode with high volumetric capacity, Front. Chem. 6 (2018) 624, https://doi.org/10.3389/fchem.2018.00624.

[29] H. Jia, X. Li, J. Song, X. Zhang, L. Luo, Y. He, B. Li, Y. Cai, S. Hu, X. Xiao, C. Wang, K.M. Rosso, R. Yi, R. Patel, J.-G. Zhang, Hierarchical porous silicon structures with extraordinary mechanical strength as high-performance lithium-ion battery anodes, Nat. Commun. 11 (1) (2020) 1474, https://doi.org/10.1038/s41467-020-15217-9.

[30] R. Gao, J. Tang, K. Zhang, K. Ozawa, L.C. Qin, A sandwich-like silicon-carbon composite prepared by surface-polymerization for rapid lithium-ion storage, Nano Energy 78 (2020) 105341, https://doi.org/10.1016/j.nanoen.2020.105341.

[31] W. Luo, C. Fang, X. Zhang, J. Liu, Hong Ma, G. Zhang, Z. Liu, X. Li, In situ generated carbon nanosheet-covered micron-sized porous Si composite for long-cycling life lithium-ion batteries, ACS Appl. Energy Mater. 4 (1) (2020) 535–544, https://doi.org/10.1021/acsaem.0c02445.

[32] Y. Zhou, Y. Yang, G. Hou, D. Yi, B. Zhou, S. Chen, T.D. Lam, F. Yuan, D. Golberg, X. Wang, Stress-relieving defects enable ultra-stable silicon anode for Li-ion storage, Nano Energy 70 (2020) 104568, https://doi.org/10.1016/j.nanoen.2020.104568.

[33] P. Sehrawat, A. Shabir, Abid, C.M. Julien, S.S. Islam, Recent trends in silicon/graphene nanocomposite anodes for lithium-ion batteries, J. Power Sources 501 (2021) 229709, https://doi.org/10.1016/j.jpowsour.2021.229709.

[34] F. Chen, J. Han, D. Kong, Y. Yuan, J. Xiao, S. Wu, D.-M. Tang, Y. Deng, W. Lv, J. Lu, F. Kang, Q.-H. Yang, 1000 Wh L^{-1} lithium-ion batteries enabled by crosslink-shrunk tough carbon encapsulated silicon microparticle anodes, Natl. Sci. Rev. (9) (2021) 8, https://doi.org/10.1093/nsr/nwab012, nwab012.

[35] M.-S. Wang, G.-L. Wang, S. Wang, J. Zhang, J. Wang, W. Zhong, F. Tang, Z.-L. Yang, J. Zheng, X. Li, In situ catalytic growth 3D multi-layers graphene sheets coated nano-silicon anode for high performance lithium-ion batteries, Chem. Eng. J. 356 (2019) 895–903, https://doi.org/10.1016/j.cej.2018.09.110.

[36] Z. Liu, Y. Zhao, R. He, W. Luo, J. Meng, Q. Yu, D. Zhao, L. Zhou, L. Mai, Yolk@Shell SiOx/C microspheres with semi-graphitic carbon coating on the exterior and interior surfaces for durable lithium storage, Energy Storage Mater. 19 (2019) 299–305, https://doi.org/10.1016/j.ensm.2018.10.011.

[37] Y. Ren, X. Yin, R. Xiao, T. Mu, H. Huo, P. Zuo, Y. Ma, X. Cheng, Y. Gao, G. Yin, Y. Li, C. Du, Layered porous silicon encapsulated in carbon nanotube cage as ultra-stable anode for lithium-ion batteries, Chem. Eng. J. 431 (2022) 133982, https://doi.org/10.1016/j.cej.2021.133982.

[38] C. Fang, J. Liu, X. Zhang, W. Luo, G. Zhang, X. Li, Z. Liu, P. Yin, W. Feng, In situ formed weave cage-like nanostructure wrapped mesoporous micron silicon anode for enhanced stable lithium-ion battery, ACS Appl. Mater. Interfaces 13 (25) (2021) 29726–29736, https://doi.org/10.1021/acsami.1c07898.

[39] Z. Hong, Z. Fang, Y. Luo, H. Wu, H. Tian, F. Zhao, Q. Li, S. Fan, J. Wang, Promising nano-silicon anodes prepared using the “disperse-anchor” strategy and functional carbon nanotube interlayers for flexible lithium-ion batteries, J. Mater. Chem. A 10 (44) (2022) 23509–23520, https://doi.org/10.1039/D2TA06478B.

[40] S.-S. Lee, K.-H. Nam, H. Jung, C.-M. Park, Si-based composite interconnected by multiple matrices for high-performance Li-ion battery anodes, Chem. Eng. J. 381 (2020) 122619, https://doi.org/10.1016/j.cej.2019.122619.

[41] Z. Fu, F. Bian, J. Ma, W. Zhang, Y. Gan, Y. Xia, J. Zhang, X. He, H. Huang, *In situ* synthesis of a Si/CNTs/C composite by directly reacting magnesium silicide with lithium carbonate for enhanced lithium storage capability, Energy Fuel. 35 (24) (2021) 20386–20393, https://doi.org/10.1021/acs.energyfuels.1c03452.

[42] T. Zhao, S. She, X. Ji, W. Jin, A. Dang, H. Li, T. Li, S. Shang, Z. Zhou, In-situ growth amorphous carbon nanotube on silicon particles as lithium-ion battery anode materials, J. Alloys Compd. 708 (2017) 500–507, https://doi.org/10.1016/j.jallcom.2017.03.019.

[43] L. Hu, X. Yan, Z. Fu, J. Zhang, Y. Xia, W. Zhang, Y. Gan, X. He, H. Huang, A “reinforced concrete” structure of silicon embedded into an in situ grown carbon nanotube scaffold as a high-performance anode for sulfide-based all-solid-state batteries, ACS Appl. Energy Mater. (2022), https://doi.org/10.1021/acsaem.2c02890 acsaem.2c02890.

[44] H. Tian, H. Tian, W. Yang, F. Zhang, W. Yang, Q. Zhang, Y. Wang, J. Liu, S.R.P. Silva, H. Liu, G. Wang, Stable hollow-structured silicon suboxide-based anodes toward high-performance lithium-ion batteries, Adv. Funct. Mater. 31 (25) (2021) 2101796, https://doi.org/10.1002/adfm.202101796.

[45] Q. Liu, D. Zhang, T. Fan, J. Gu, Y. Miyamoto, Z. Chen, Amorphous carbon-matrix composites with interconnected carbon nano-ribbon networks for electromagnetic interference shielding, Carbon 46 (3) (2008) 461–465, https://doi.org/10.1016/j.carbon.2007.12.010.

[46] J.-Y. Li, G. Li, J. Zhang, Y.-X. Yin, F.-S. Yue, Q. Xu, Y.-G. Guo, Rational design of robust Si/C microspheres for high-tap-density anode materials, ACS Appl. Mater. Interfaces 11 (4) (2019) 4057–4064, https://doi.org/10.1021/acsami.8b20213.

[47] L. Hou, H. Zheng, R. Cui, Y. Jiang, Q. Li, X. Jiang, J. Gao, F. Gao, Silicon carbon nanohybrids with expandable space: a high-performance lithium battery anodes, Microporous Mesoporous Mater. 275 (2019) 42–49, https://doi.org/10.1016/j.micromeso.2018.08.014.

[48] B. Bulut Kopuklu, A. Tasdemir, S. Alkan Gursel, A. Yurum, High stability graphene oxide aerogel supported ultrafine Fe_3O_4 particles with superior performance as a Li-ion battery anode, Carbon 174 (2021) 158–172, https://doi.org/10.1016/j.carbon.2020.12.049.

[49] P.-W. Chi, T. Paul, Y.-H. Su, K.-H. Su, C.-Y. Su, P.M. Wu, S.-F. Wang, M.-K. Wu, A study on Ti-doped Fe_3O_4 anode for Li ion battery using machine learning, electrochemical and distribution function of relaxation times (DFRTs) analyses, Sci. Rep. 12 (1) (2022) 4851, https://doi.org/10.1038/s41598-022-08584-4.

[50] G. Greenidge, S. Price, J. Erlebacher, Carbon transformations in rapidly solidified nickel–carbon ribbon, Carbon 184 (2021) 669–679, https://doi.org/10.1016/j.carbon.2021.08.037.

[51] Y. Li, K. Yan, H.-W. Lee, Z. Lu, N. Liu, Y. Cui, Growth of conformal graphene cages on micrometre-sized silicon particles as stable battery anodes, Nat. Energy 1 (2) (2016) 15029, https://doi.org/10.1038/nenergy.2015.29.

[52] N. Liu, Z. Lu, J. Zhao, M.T. McDowell, H.-W. Lee, W. Zhao, Y. Cui, A pomegranate-inspired nanoscale design for large-volume-change lithium battery anodes, Nat. Nanotechnol. 9 (3) (2014) 187–192, https://doi.org/10.1038/nnano.2014.6.

[53] M. Miyachi, H. Yamamoto, H. Kawai, T. Ohta, M. Shirakata, Analysis of SiO anodes for lithium-ion batteries, J. Electrochem. Soc. 152 (10) (2005) A2089, https://doi.org/10.1149/1.2013210.
[54] J. Lee, S.A. Han, S.-M. Lee, M.-S. Park, J.H. Kim, Electrochemical properties of nonstoichiometric silicon suboxide anode materials with controlled oxygen concentration, Composites, Part B 174 (2019) 107024, https://doi.org/10.1016/j.compositesb.2019.107024.
[55] C. He, S. Wu, N. Zhao, C. Shi, E. Liu, J. Li, Carbon-encapsulated Fe_3O_4 nanoparticles as a high-rate lithium ion battery anode material, ACS Nano 7 (5) (2013) 4459–4469, https://doi.org/10.1021/nn401059h.
[56] M.D. Goodman, S. Kim, N. Tatsuda, K. Yano, P.V. Braun, Enhanced secondary battery anodes based on Si and Fe_3O_4 nanoparticle infilled monodisperse carbon starburst colloidal crystals, Part. Part. Syst. Char. 32 (10) (2015) 928–933, https://doi.org/10.1002/ppsc.201500081.
[57] Y. Ma, J. Huang, X. Liu, F. Bu, L. Wang, Q. Xie, D.-L. Peng, 3D graphene-encapsulated hierarchical urchin-like Fe_3O_4 porous particles with enhanced lithium storage properties, Chem. Eng. J. 327 (2017) 678–685, https://doi.org/10.1016/j.cej.2017.06.147.
[58] W. Wei, S. Yang, H. Zhou, I. Lieberwirth, X. Feng, K. Müllen, 3D graphene foams cross-linked with pre-encapsulated Fe_3O_4 nanospheres for enhanced lithium storage, Adv. Mater. 25 (21) (2013) 2909–2914, https://doi.org/10.1002/adma.201300445.
[59] L. Liu, X. Yang, C. Lv, A. Zhu, X. Zhu, S. Guo, C. Chen, D. Yang, Seaweed-derived route to Fe_2O_3 hollow nanoparticles/N-doped graphene aerogels with high lithium ion storage performance, ACS Appl. Mater. Interfaces 8 (11) (2016) 7047–7053, https://doi.org/10.1021/acsami.5b12427.
[60] L. Su, Y. Zhong, Z. Zhou, Role of transition metal nanoparticles in the extra lithium storage capacity of transition metal oxides: a case study of hierarchical core–shell Fe_3O_4@C and Fe@C microspheres, J. Mater. Chem. A 1 (47) (2013) 15158, https://doi.org/10.1039/c3ta13233a.
[61] T. Yuan, Y. Jiang, W. Sun, B. Xiang, Y. Li, M. Yan, B. Xu, S. Dou, Ever-increasing pseudocapacitance in RGO–MnO–RGO sandwich nanostructures for ultrahigh-rate lithium storage, Adv. Funct. Mater. 26 (13) (2016) 2198–2206, https://doi.org/10.1002/adfm.201504849.